

# Polarization-resolved black phosphorus/molybdenum disulfide mid-wave infrared photodiodes with high detectivity at room temperature

James Bullock<sup>1,2,6</sup>, Matin Amani<sup>1,2,6</sup>, Joy Cho<sup>1,2</sup>, Yu-Ze Chen<sup>3</sup>, Geun Ho Ahn<sup>1,2</sup>, Valerio Adinolfi<sup>1,2</sup>, Vivek Raj Shrestha<sup>4</sup>, Yang Gao<sup>5</sup>, Kenneth B. Crozier<sup>4,5</sup>, Yu-Lun Chueh<sup>3</sup> and Ali Javey<sup>1,2\*</sup>

**Infrared photodetectors are currently subject to a rapidly expanding application space, with an increasing demand for compact, sensitive and inexpensive detectors. Despite continued advancement, technological factors limit the widespread usage of such detectors, specifically, the need for cooling and the high costs associated with processing of III-V/II-VI semiconductors. Here, black phosphorous (bP)/MoS<sub>2</sub> heterojunction photodiodes are explored as mid-wave infrared (MWIR) detectors. Although previous studies have demonstrated photodiodes using bP, here we significantly improve the performance, showing that such devices can be competitive with conventional MWIR photodetectors. By optimizing the device structure and light management, we demonstrate a two-terminal device that achieves room-temperature external quantum efficiencies ( $\eta_e$ ) of 35% and specific detectivities ( $D^*$ ) as high as  $1.1 \times 10^{10} \text{ cm Hz}^{1/2} \text{ W}^{-1}$  in the MWIR region. Furthermore, by leveraging the anisotropic optical properties of bP we demonstrate the first bias-selectable polarization-resolved photodetector that operates without the need for external optics.**

Infrared photodetectors are essential components in a host of fields, including medical, scientific, communication, automation and surveillance<sup>1,2</sup>. The majority of today's commercially available, high-performance infrared photodetectors are made using III-V and II-VI absorbers, such as In<sub>1-x</sub>Ga<sub>x</sub>As, InSb and Hg<sub>1-x</sub>Cd<sub>x</sub>Te (ref. <sup>3</sup>). Although significant progress has greatly increased their application, a number of drawbacks limit the wider utilization of infrared photodetectors. Most notably, these devices typically rely on expensive growth methods and require active cooling to reduce thermal noise. The latter is particularly crucial for narrow-bandgap absorbers operating in the mid-wave infrared (MWIR, 3–5  $\mu\text{m}$ ) and long-wave infrared (LWIR, 8–12  $\mu\text{m}$ ) spectral bands, where cryogenic cooling is typically required to achieve high performance. In addition, several specific applications cannot be directly addressed using detectors fabricated from traditional material systems. An example of this is detection of the polarization state of light, which is utilized in numerous specialized applications including astronomy, polarization-division multiplexing and remote sensing. Normally, detectors used for this application require either polarization optics or multiple devices arranged in a side-by-side configuration, which adds system complexity and limits the resolution for imaging purposes. Furthermore, while numerous materials, most notably nanowires, show polarized absorption, a polarization-resolved detector has yet to be demonstrated. As such, there is considerable interest in the exploration of new infrared absorber materials that offer the potential to address these shortcomings and can be applied in novel device architectures.

Two-dimensional (2D) materials have shown initial promise for use in future infrared photodetectors<sup>4,5</sup>. One of the key advantages

offered by 2D layered crystals is their out-of-plane van der Waals bonding, which allows the use of thin layers without detrimental effects such as surface dangling bonds. This advantage is particularly important in infrared detectors where thin absorbers can reduce noise resulting from generation-recombination, a strategy that is often not permitted in traditional semiconductors due to surface recombination. Furthermore, the van der Waals bonding in these materials allows for the construction of heterojunctions without consideration of factors such as lattice matching or deposition temperature, providing a significant advantage over traditional 3D materials. Black phosphorus (bP), an elemental 2D material, has recently garnered a significant amount of attention within the optoelectronic community<sup>5–7</sup>. This interest is partially based on the anisotropic optoelectronic properties of bP, which result in polarization-dependent absorption<sup>7,8</sup>. Black phosphorus also exhibits a thickness-tunable direct bandgap, between the near-infrared ( $E_g \approx 1.5 \text{ eV}$ ) for monolayers to the MWIR ( $E_g \approx 0.3 \text{ eV}$ ) for bulk<sup>7,8</sup>. In addition, several studies have demonstrated that bP can be effectively combined with transition metal dichalcogenides such as MoS<sub>2</sub> (refs <sup>9–11</sup>), WSe<sub>2</sub> (ref. <sup>12</sup>) and ReS<sub>2</sub> (ref. <sup>13</sup>) to form a range of functional van der Waals heterojunctions. So far, numerous photodetectors utilizing bP have been demonstrated, indicating its promise as a next-generation infrared detector platform<sup>14–16</sup>. Among these, a number of preliminary studies have shown the potential of the bP/MoS<sub>2</sub> heterojunction in this application<sup>9–11</sup>. However, devices presented thus far show inferior performance to existing infrared room-temperature photodetectors, with reported external quantum efficiency values of less than 5%, and are characterized only at discrete wavelengths either in the near-infrared or short-wave infrared bands.

<sup>1</sup>Department of Electrical Engineering and Computer Sciences, University of California, Berkeley, CA, USA. <sup>2</sup>Materials Sciences Division, Lawrence Berkeley National Laboratory, Berkeley, CA, USA. <sup>3</sup>Department of Materials Science and Engineering, National Tsing Hua University, Hsinchu, Taiwan, Republic of China. <sup>4</sup>School of Physics, University of Melbourne, Melbourne, Victoria, Australia. <sup>5</sup>Department of Electrical and Electronic Engineering, University of Melbourne, Melbourne, Victoria, Australia. <sup>6</sup>These authors contributed equally: James Bullock, Matin Amani. \*e-mail: [ajavey@berkeley.edu](mailto:ajavey@berkeley.edu)

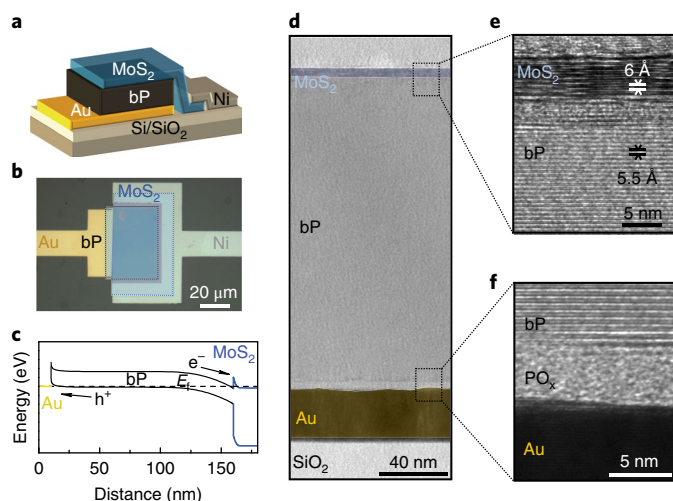


**Fig. 1 | bP/MoS<sub>2</sub> heterojunction photodiode concept.** **a**, Schematic of device configuration, showing the heterojunction and contact configuration. **b**, Optical micrograph of a completed device; regions containing bP and MoS<sub>2</sub> are outlined for clarity. **c**, Simulated energy band diagram of the device under equilibrium. **d**, Cross-sectional TEM image of a completed photodiode. **e**, High-resolution cross-sectional TEM image showing the bP/MoS<sub>2</sub> interface. **f**, High-resolution cross-sectional TEM image showing the bP/Au interface.

Here, we utilize bP/MoS<sub>2</sub> heterostructures to fabricate photodiodes and optimize the devices for detection of MWIR light intensity and polarization at room temperature. To optimize the collection of light, we performed in-depth characterization of bP, and report the complex refractive index of this material in a wavelength range that encompasses the MWIR. This information is used to design and fabricate a simple optical structure that deliberately utilizes destructive interference to efficiently couple in a narrow band of MWIR light, permitting the demonstration of a high-quantum-efficiency bP/MoS<sub>2</sub> photodiode. Finally, we demonstrate a bias-selectable polarization-resolved bP photodetector, utilizing two orthogonally aligned bP/MoS<sub>2</sub> photodiodes, monolithically integrated to create a device that directly measures both the intensity and polarization of incoming MWIR light.

## Results and discussion

**Black phosphorus MWIR photodiode design.** Two primary figures of merit for photodetectors are their external quantum efficiency ( $\eta_e$ ) and specific detectivity ( $D^*$ ). These parameters are optimized by increasing the percentage of incident photons that generate photocurrent as well as via reduction of the electronic noise. As such, simultaneous optimization of  $\eta_e$  and  $D^*$  requires consideration of both the optical and electrical design. A schematic showing the structure of the heterojunction photodiodes fabricated in this work as well as an example optical micrograph are shown in Fig. 1a,b, respectively. The device consists of a bP/MoS<sub>2</sub> heterojunction in which a thin (~10–20 nm) n-type MoS<sub>2</sub> layer acts as an electron-selective contact and MWIR window. Holes are contacted via a rear Au pad, which simultaneously acts as a MWIR back reflector. As shown schematically in the simulated band diagram of Fig. 1c, the MoS<sub>2</sub> heterojunction provides asymmetric band offsets with the bP, allowing the flow of electrons to the MoS<sub>2</sub> contact while blocking the flow of holes. A false-coloured transmission electron micrograph (TEM) of a completed device is shown in Fig. 1d. In addition, high-resolution TEM images of the bP/MoS<sub>2</sub> and bP/Au interfaces are shown in Fig. 1e,f, respectively. The layered structure of bP and MoS<sub>2</sub> can be seen with corresponding monolayer thicknesses of 5.5 and 6 Å, respectively. A thin amorphous layer

can also be observed at both interfaces, most prominently at the bP/Au interface. This is attributed to PO<sub>x</sub> from surface oxidation, which forms during periods of atmospheric exposure while fabricating devices<sup>6</sup>. This layer could introduce adverse effects to the device performance, particularly to the collection efficiency as it obscures the selective contacts, and its response time, due to the defective nature of the PO<sub>x</sub> layer.

**Refractive index extraction and optical optimization.** Losses due to reflection limit the fraction of incident light that can be absorbed and are a strong function of both the bP and MoS<sub>2</sub> layer thicknesses. Reflection and absorption in the device can be modelled using the complex refractive index ( $n$ ,  $k$ ) of the two materials. Although broadband values of  $n$  and  $k$  have been reported for MoS<sub>2</sub>, only the visible refractive index has been characterized for bP so far<sup>17</sup>. The anisotropic crystalline structure of bP, shown in Fig. 2a, results in polarization-dependent optical properties (referred to as linear dichroism). Light impinging with an electrical field parallel to the  $x$  axis (the armchair direction) sees a sharp absorption onset at the bulk bP band edge of ~0.31 eV (refs <sup>6,7,18</sup>). Absorption of polarized light aligned to the  $y$  axis (the zigzag direction), however, is symmetry-forbidden at the ~0.31 eV band edge and substantially weaker at higher-energy wavelengths<sup>7,8,19</sup>. This has been confirmed experimentally for bulk bP from MWIR to visible wavelengths<sup>5,7,20</sup>. To extract an effective  $n$  and  $k$  for the  $x$  and  $y$  directions in bP, polarized reflection measurements were performed on bP crystals with thickness ranging from 50 to 500 nm on Au substrates. Example reflection data at different individual thicknesses are provided in Supplementary Section 1. The combined interpolation of these polarized reflection measurements is shown in Fig. 2b,c for incident polarizations aligned along the  $x$  and  $y$  axes of bP, respectively.

For polarized illumination aligned in the  $x$  direction, a clear drop in reflection can be seen at photon energies above 0.31 eV for all thicknesses. This is a result of the onset of absorption at the band edge of bP. As expected, no such sharp step is seen for the  $y$  direction in Fig. 2c. Refractive index values were obtained using the transfer matrix method<sup>21</sup> to fit a model of the thickness ( $t$ ) dependent reflection  $R_{\text{model}}(t)$  to the measured reflection  $R_{\text{meas}}(t)$  at each wavelength. The model is based on a bP/Au stack and assumes that the refractive index is independent of thickness across the measured thickness range (50–500 nm). This assumption is based on the predicted saturation of the layer-dependent band-structure of bP above ~8 layers<sup>6</sup>, and is also demonstrated by fitted reflection measurements in Supplementary Section 1. The extracted  $n$  and  $k$  values for the  $x$  and  $y$  directions are provided in Fig. 2d,e, respectively. For light polarized in the  $x$  direction, a pronounced step in extinction coefficient  $k$  is observed at  $\lambda = 3.8 \mu\text{m}$ , which corresponds well to the expected band edge of bP. More details of the indices extraction process are provided in Supplementary Section 1.

With these  $n$  and  $k$  values, we used the transfer matrix method to simulate the absorption of the photodiode in the  $x$  direction. Ideally, from an electrical standpoint, the thickness of the bP layer should be minimized to reduce noise resulting from generation–recombination as well as to improve the carrier extraction efficiency. However, from an optical perspective, absorption within the bP layer, which is small for very thin layers, should be maximized. To obtain a compromise between these two requirements, the bP absorption, averaged between  $\lambda = 2.5$  and  $3.8 \mu\text{m}$ , is simulated as a function of the bP and MoS<sub>2</sub> layer thicknesses. A contour plot of the modelled absorption is provided in Fig. 2f. The periodic absorption behaviour is associated with changes in front surface reflection due to thickness-dependent constructive and destructive interference of MWIR light. A local maximum in absorption is seen for bP layers

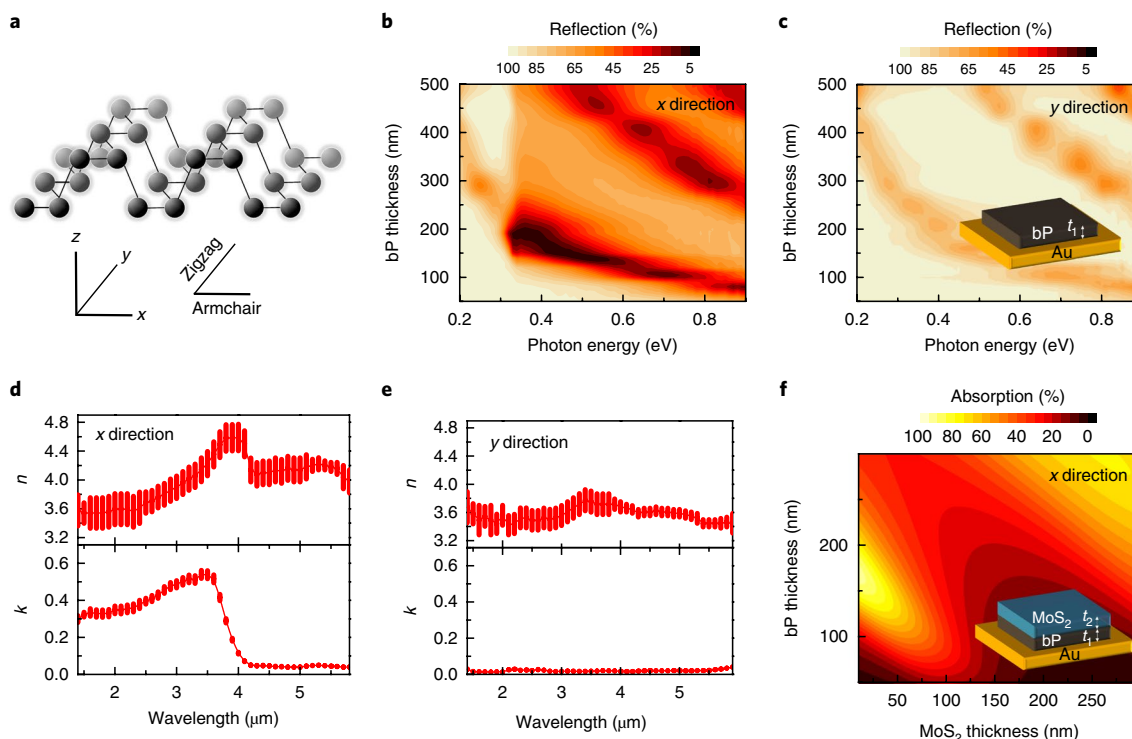


**Fig. 2 | Infrared optical constants of bP.** **a**, Schematic diagram of bP crystal structure. **b**, Reflection of bP on Au, measured for crystals with thickness ranging from 50 to 500 nm with the polarizer aligned in the x direction. **c**, Reflection of bP on Au, measured for crystals with thickness ranging from 50 to 500 nm with the polarizer aligned in the y direction. **d**, Extracted complex refractive index of bP in the x direction. **e**, Extracted complex refractive index of bP in the y direction. Error bars in **d** and **e** are based on the deviation between the modelled and measured reflection at each wavelength. **f**, Modelled absorption in the bP layer, for a bP/MoS<sub>2</sub> stack on Au, as a function of bP and MoS<sub>2</sub> layer thicknesses.

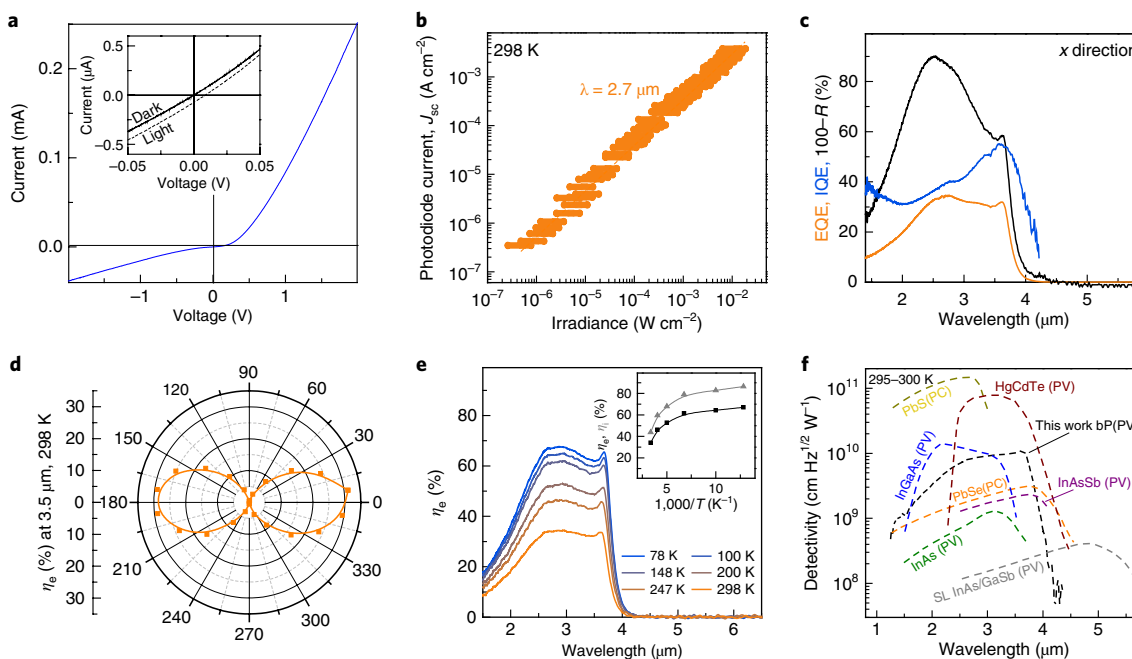


**Fig. 3 | Photoresponse and detectivity.** **a**,  $I$ - $V$  curve of a bP/MoS<sub>2</sub> heterojunction photodiode. Inset: measurement taken in the dark and under illumination by a 1,000 K blackbody source. **b**, Measured photocurrent as a function of incident illumination intensity. Excitation is performed with a  $\lambda = 2.7 \mu\text{m}$  laser diode. Error bars represent uncertainty in the laser spot size. **c**, Spectrally dependent  $\eta_e$ ,  $\eta_i$  and 100%- $R$  for a bP/MoS<sub>2</sub> heterojunction photodiode. **d**, Measured  $\eta_e$  at  $\lambda = 3.5 \mu\text{m}$  as a function of polarization angle. **e**, Spectral  $\eta_e$  as a function of temperature. Inset:  $\eta_e$  and  $\eta_i$  at  $\lambda = 3 \mu\text{m}$  as a function of temperature. **f**, Specific detectivity as a function of wavelength measured for a bP/MoS<sub>2</sub> heterojunction at room temperature as well as various commercially available and reported MWIR photovoltaic (PV) and photoconductive (PC) detectors. All FTIR and laser diode characterization was performed at a bias of 0 V.

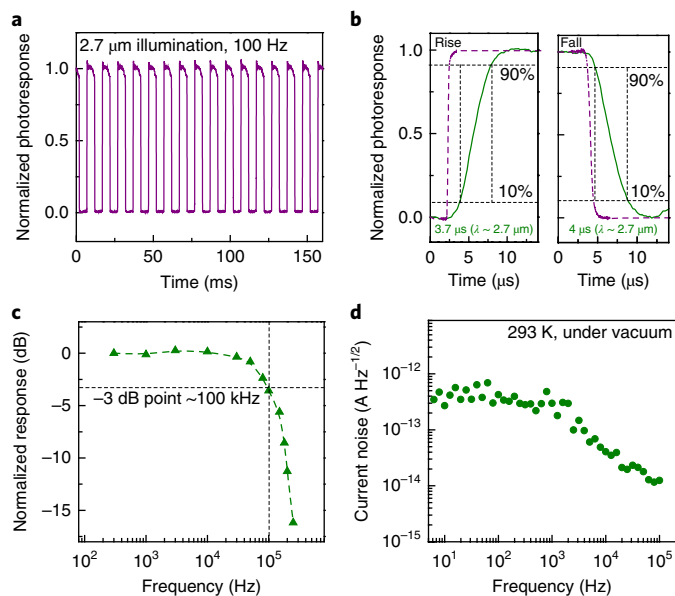


**Fig. 4 | Frequency response and noise.** **a**, Photocurrent measured from a bP/MoS<sub>2</sub> photodiode under a modulated illumination source ( $\lambda = 2.7 \mu\text{m}$ ). **b**, 90–10% rise and fall times measured with a  $\lambda = 2.7 \mu\text{m}$  illumination source ( $\sim 10 \text{ mW cm}^{-2}$ ). Green solid lines are representative of the bP/MoS<sub>2</sub> photodiode and purple dashed lines show the instrument response (measured using a commercial InAs photodiode, Judson J12D). **c**, Frequency response of a bP/MoS<sub>2</sub> photodiode, showing a 3-dB frequency of 100 kHz ( $\lambda = 1.6 \mu\text{m}$ ). **d**, Spectral noise density of a bP/MoS<sub>2</sub> photodiode. All device photoresponse and noise characterization was performed at a bias of 0 V.

with a thickness of 170 nm on Au, with an MoS<sub>2</sub> thickness of zero. This corresponds to the expected quarter wavelength minima in reflection, and hence interference effects can be used to provide a compromise between minimizing the thickness and maximizing absorption. Given that an MoS<sub>2</sub> layer with sufficient lateral conductivity is required to collect electrons, we chose an optimum device configuration of bP ( $\sim 150 \text{ nm}$ )/MoS<sub>2</sub> (15 nm). With this optical design,  $\sim 80\%$  of incident light polarized in the  $x$  direction at  $\lambda = 3 \mu\text{m}$  can be absorbed in the bP layer. We emphasize that, in terms of device thickness, this detector bridges the gap between conventional 2D material photodetectors and traditional bulk semiconductor detectors. As a result, it inherits benefits from both detector classes, such as increased absorption, as well as being free of surface dangling bonds.

**Photodiode characterization.** The  $I$ – $V$  characteristics of a typical bP/MoS<sub>2</sub> heterojunction photodiode, measured at 300 K with no illumination, are shown in Fig. 3a and show the expected rectifying behaviour of a diode formed using a narrow-bandgap material. The inset of Fig. 3a compares the measured  $I$ – $V$  behaviour with and without illumination from a 1,000 K unpolarized blackbody source. The generation of photocarriers shifts the  $I$ – $V$  curve downwards, resulting in an open-circuit voltage  $V_{oc}$  and short-circuit current  $I_{sc}$ , confirming that the device is operating in the photovoltaic mode. Figure 3b shows the relationship between the short-circuit current density  $J_{sc}$  and incident optical power density from a  $\lambda = 2.7 \mu\text{m}$  laser diode source. The device shows the expected linear increase in photocurrent as a function of incident light power density over the full measurement range, which spans five orders of magnitude. Similar results were found using a  $\lambda = 1.6 \mu\text{m}$  illumination source, as shown in Supplementary Section 5.

The quantum efficiency of the device was measured for  $x$  direction polarized illumination using a calibrated Fourier-transform infrared spectrometer (FTIR), the set-up of which is described in the Methods. As shown in Fig. 3c, the bP/MoS<sub>2</sub> photodiode shows an external quantum efficiency  $\eta_e$  of  $\sim 30$ – $35\%$  for  $\lambda = 2.5$ – $3.5 \mu\text{m}$ . These are the highest  $\eta_e$  values reported for bP in this range at room temperature and correspond to current responsivity values of  $\sim 0.9 \text{ A W}^{-1}$  (Supplementary Section 3). Also presented in Fig. 3c is the measured reflection  $R$ , plotted as  $100\% - R$ . The narrow spectral band of MWIR light coupled into the absorber corresponds to the targeted quarter wavelength interference feature with a peak occurring just below  $\lambda = 3 \mu\text{m}$ . From  $\eta_e$  and  $R$ , the internal quantum efficiency ( $\eta_i$ ) can also be calculated according to  $\eta_i(\lambda) = \eta_e(\lambda) / (100 - R(\lambda))$ , yielding a value of 40–50% at room temperature. The polarization dependence of  $\eta_e$  at  $\lambda = 3.5 \mu\text{m}$ , as a function of polarization angle, is provided in the polar plot of Fig. 3d. It can be seen that as the polarization angle is changed from  $0^\circ$  (aligned with the  $x$  axis) to  $90^\circ$  (aligned with the  $y$  axis), a decrease in  $\eta_e$ , from greater than 30% to less than 1%, is measured. An example  $\eta_e(\lambda)$  comparison across the MWIR spectral range for these two polarization angles is provided in Supplementary Section 3. That the  $\eta_e$  for  $x$ -polarized light is substantially higher than for  $y$ -polarized light is consistent with the anisotropic absorption discussed in Fig. 2 and is in alignment with previous responsivity measurements of bP photodetectors at shorter wavelengths<sup>7</sup>.

As shown in Fig. 3e,  $\eta_e$  shows no significant changes in spectral shape as a function of temperature, apart from a small redshift in the absorption edge, attributed to a decrease in the bandgap with decreasing temperature. This anomalous temperature dependence of the bandgap has been previously predicted and experimentally observed in bP<sup>22,23</sup>. However,  $\eta_e$  increases as the temperature is decreased, reaching a value of 63% at 78 K. This is further illustrated in the inset of Fig. 3c, with  $\eta_e$  and  $\eta_i$  (measured at  $\lambda = 3 \mu\text{m}$ ) plotted as a function of inverse temperature, showing that  $\eta_i$  reaches a peak value of 84% at 100 K. This is probably a result of an increase in the minority carrier diffusion length at lower temperatures, which in turn increases the collection efficiency of the back contact. A previously measured increase in the mobility of bP at low temperatures ( $\mu_{h,300\text{K}} \approx 750 \text{ cm}^2 \text{ V}^{-1} \text{ s}^{-1}$ ,  $\mu_{h,77\text{K}} \approx 3,800 \text{ cm}^2 \text{ V}^{-1} \text{ s}^{-1}$ )<sup>24</sup> can partially account for this predicted increasing diffusion length.

To directly compare the performance of the bP/MoS<sub>2</sub> photodiode to conventional photodetectors, we extracted its specific detectivity  $D^*$ . This was achieved with two independent approaches, as discussed in detail in the Methods. First,  $D^*$  is calculated following the approach suggested in ref. <sup>3</sup> (for a photodiode under 0 V bias) from  $\eta_e$  and the zero-bias resistance area product ( $R_0A$ ):

$$D^* = \frac{\eta_e \lambda q}{hc} \left( \frac{4kT}{R_0A} + 2q^2 \eta_e \Phi_b \right)^{-1/2} \quad (1)$$

where  $\lambda$  is the wavelength,  $q$  is the elementary charge,  $c$  is the speed of light in vacuum,  $T$  is the detector temperature,  $\Phi_b$  is the background flux density, and  $h$  and  $k$  are the Planck and Boltzmann constants. The second term in parentheses accounts for contributions to noise from fluctuations in the thermal background and is negligible in this case, as  $4kT/R_0A > 2q^2 \eta_e \Phi_b$ . Figure 3f shows  $D^*(\lambda)$  extracted from this approach at room temperature compared against current state-of-the-art room-temperature photodiodes<sup>25,26</sup>, many of which are commercially available. It can be seen that the bP photodiode outperforms more established technologies in the MWIR region, with a peak  $D^*$  of  $1.1 \times 10^{10} \text{ cm Hz}^{1/2} \text{ W}^{-1}$  at  $\lambda = 3.8 \mu\text{m}$ . It should be noted that the MoS<sub>2</sub>/bP photodiode presented in Fig. 3 has been characterized at 0 V bias, unlike many of the detectors presented in Fig. 3f, which require an applied bias to obtain the reported values. To verify the MoS<sub>2</sub>/bP photodiode  $D^*$  values, the noise equivalent power

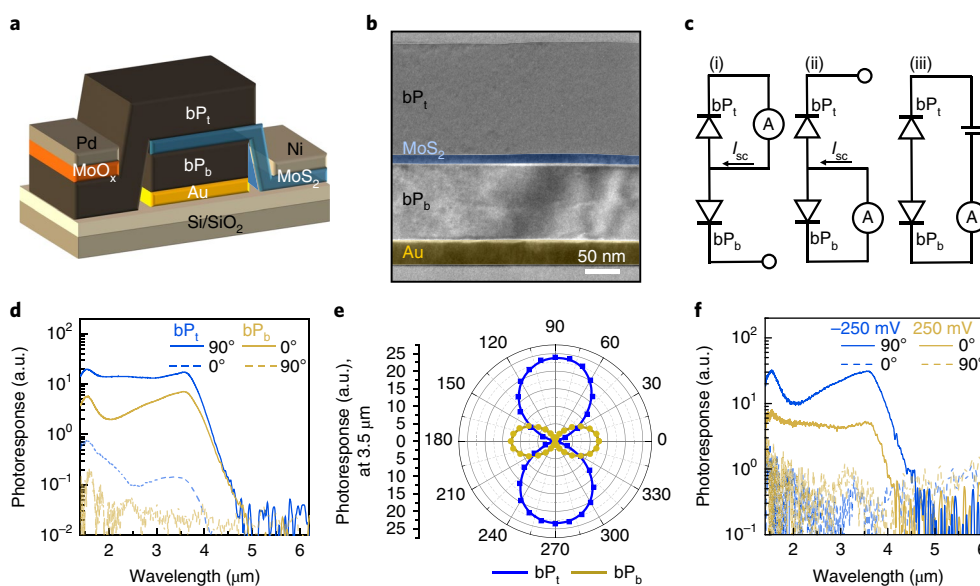


**Fig. 5 | Polarization-resolved bP/MoS<sub>2</sub> heterojunction photodiode.** **a**, Schematic of polarization-resolved bP/MoS<sub>2</sub> heterojunction photodiode, showing the heterojunction and contact configuration. **b**, Cross-sectional TEM image of a completed polarization-resolved bP/MoS<sub>2</sub> heterojunction photodetector, showing the various layers in the device. **c**, Electrical configurations used to measure: photoresponse from bP<sub>t</sub> (i), photoresponse from bP<sub>b</sub> (ii) and photoresponse from the top or bottom mode using the bias-selectable mode (iii). **d**, Spectrally resolved photoresponse measured from bP<sub>t</sub> and bP<sub>b</sub> under linearly polarized illumination normal and perpendicular to the device. **e**, Measured photoresponse under linearly polarized illumination at  $\lambda = 3 \mu\text{m}$  in bP<sub>t</sub> and bP<sub>b</sub> as a function of polarizer angle. **f**, Spectrally resolved photoresponse of the device in the bias-selectable mode under four different conditions:  $\pm 250 \text{ mV}$  for polarization aligned to the  $x$  axis of the top and bottom devices.

(NEP) was measured for this device under flood illumination from a blackbody source as described in Supplementary Section 4. In this approach the incident power density is calculated using geometrical considerations, the temperature of the source and integration of the total irradiance to the band edge<sup>27</sup>. Additionally, the noise is directly measured allowing  $D^*$  to be calculated as  $\sqrt{A\Delta f}/\text{NEP}$ , where  $\Delta f$  is the integration time (1 s) and  $A$  is the area. From this measurement, we find a room-temperature  $D^*$  value of  $7 \times 10^9 \text{ cm Hz}^{1/2} \text{ W}^{-1}$ . This value is in good agreement with the spectral  $D^*$  calculated from the device  $R_p A$  shown in Fig. 3f. Further information on  $D^*$  for these detectors, including its temperature dependence, is provided in Supplementary Sections 3 and 4.

The frequency response and noise current for the bP/MoS<sub>2</sub> heterojunction photodiodes are characterized in Fig. 4. As shown in Fig. 4a, no observable baseline drift in photoresponse is observed under modulated laser diode illumination ( $\lambda = 2.7 \mu\text{m}$ ). In addition, the rise and fall times, measured under  $\lambda = 2.7 \mu\text{m}$  illumination at 0 V bias, are found to be  $3.7 \mu\text{s}$  and  $4 \mu\text{s}$ , respectively, as shown in Fig. 4b. These values are among the fastest reported for bP-based photoconductors and photodiodes<sup>14,16,28</sup>. Although this is slower than commercially available MWIR photodiodes<sup>29</sup>, these values are promising given the early stage of device development, and are faster than common photoconductive and thermal detectors, as shown in Supplementary Table 2. Improvements in response time could be achieved by reducing the bP bulk trap concentration during crystal growth and eliminating defective PO<sub>x</sub> interfacial layers by developing an oxidant-free fabrication procedure. The dashed purple lines in Fig. 4b, measured from a commercially available InAs photodiode, are included to provide a reference of the instrument response. Similar rise/fall times are found when an illumination source of  $\lambda = 1.6 \mu\text{m}$  is used, as shown in Supplementary Section 5. Figure 4c shows the measured frequency response, with the 3 dB point at  $\sim 100 \text{ kHz}$ , using a  $\lambda = 1.6 \mu\text{m}$  illumination source. Figure 4d shows the measured noise current spectrum of the bP/MoS<sub>2</sub> photodiode. The shape it exhibits is commonly seen in systems dominated by generation–recombination noise and, notably,  $1/f$  noise behaviour

is not observed at low frequencies because the device is operated in photovoltaic mode at zero bias<sup>30</sup>. The measured low-frequency noise has a value of  $4 \times 10^{-13} \text{ A Hz}^{-1/2}$ . This is similar but higher than that reported previously for photodiodes fabricated using black phosphorus–arsenic alloys (bPAs), which exhibit low-frequency noise of  $\sim 7 \times 10^{-14} \text{ A Hz}^{-1/2}$ . This difference can be attributed to the thicker absorber layer ( $\sim 150 \text{ nm}$ ) used in this work in comparison with the devices in ref. <sup>31</sup> (5–20 nm), which results in lower generation–recombination noise.

**Polarization-resolved, bias-selectable photodetector.** Finally, we leverage the device structure and anisotropic optical properties of bP to develop a polarization-resolved detector. A schematic of the polarization-resolved detector developed in this study is shown in Fig. 5a and a false-coloured TEM cross-section of a fabricated device is shown in Fig. 5b. The device consists of two vertically stacked bP layers arranged so that their crystal orientations are perpendicular to one another. These two bP layers are separated by a common MoS<sub>2</sub> electron contact and each bP layer has an isolated hole contact. This configuration is similar to the two-colour back-to-back photodiodes that have been previously demonstrated with III–V semiconductors<sup>32</sup>. The bottom bP layer utilizes a full-area Au hole contact, similar to the photodiodes presented above, while the top bP layer collects holes through a MoO<sub>x</sub>/Pd hole contact adjacent to the back reflector. The MoO<sub>x</sub>/Pd stack has been shown to be an effective hole contact to a number of semiconductor materials<sup>33,34</sup> because of its large work function.

To demonstrate the performance of this device, spectrally resolved photoresponse measurements were taken individually on the top and bottom bP photodetectors using the circuit configuration shown in Fig. 5c (i) and (ii), respectively. Each device was measured under two conditions: linearly polarized light aligned to the  $x$  axis of the top device ( $90^\circ$ ) and linearly polarized light aligned to the  $x$  axis of the bottom device ( $0^\circ$ ). All four measurements are shown in Fig. 5d. The performance of this device can be quantified by an extinction ratio  $r_e$  for each layer, defined as the photoresponse

measured with  $x$ -polarized illumination divided by the photoresponse with  $y$ -polarized illumination. For both the top and bottom devices,  $r_c$  values of  $\sim 100:1$  were calculated at  $\lambda = 3.5 \mu\text{m}$ , which is on the order of the extinction ratio of the polarizer used in this study. These results were further corroborated by the polar plot of Fig. 5e, which shows the photoresponse as a function of polarizer angle at  $\lambda = 3.5 \mu\text{m}$ . In separate measurements, presented in Supplementary Section 6, the device is also shown to be able to simultaneously detect the two linear polarization components when illuminated with unpolarized light. Furthermore, the response from the individual detectors can be accessed in a bias-selectable (two-terminal) configuration as depicted in the circuit schematic of Fig. 5c (iii). By applying a bias of  $\pm 250 \text{ mV}$  across the outer contacts, one device is reverse-biased (where the photocurrent is collected) and the other forward-biased (contributing negligibly to the photocurrent). Note that for these measurements the  $\text{MoS}_2$  contact was electrically disconnected. The functionality of this configuration is clearly seen in Fig. 5f by the exclusive collection of only  $0^\circ$  or  $90^\circ$  linearly polarized MWIR light under negative or positive biasing, respectively. A bias of  $\pm 250 \text{ mV}$  was chosen as it was the minimum value at which photocurrent from the two detectors could be effectively separated. Higher biases were avoided to minimize noise due to dark current in the device. The unbalanced photocurrent from the top and bottom bP layers can be attributed to a combination of device variation and differences in absorption arising from the layer thicknesses and their position within the device stack. An optical structure, which couples in and absorbs an equal proportion of perpendicularly polarized light in the two bP absorbers, can be realized by controlling the bP and  $\text{MoS}_2$  layer thicknesses and integrating an antireflection layer.

## Conclusion

In summary, we have designed and fabricated MWIR bP/ $\text{MoS}_2$  heterojunction photodiodes with high performance at room temperature. By determining the complex refractive index in the infrared, we have designed a simple optical structure for the bP/ $\text{MoS}_2$  photodiode that achieves high MWIR absorption via interference. This allows the use of a moderately thin bP layer ( $\sim 150 \text{ nm}$ ), which reduces noise while still permitting high absorption (in excess of  $\sim 80\%$ ) within a narrow band in the MWIR region. These devices display impressive room-temperature  $\eta_c$  and  $D^*$  values of 35% and  $1.1 \times 10^{10} \text{ cm Hz}^{1/2} \text{ W}^{-1}$ , respectively. Finally, we utilize the anisotropic optical properties of bP to demonstrate a bias-selectable polarization-resolved monolithic photodetector, which is capable of simultaneously detecting orthogonally polarized light without the use of external optics. This could further be expanded to create polarimetry focal plane arrays that do not rely on moving parts or additional optical components.

## Methods

Methods, including statements of data availability and any associated accession codes and references, are available at <https://doi.org/10.1038/s41566-018-0239-8>.

Received: 12 November 2017; Accepted: 23 July 2018;  
Published online: 27 August 2018

## References

- Xia, F., Wang, H., Xiao, D., Dubey, M. & Ramasubramanian, A. Two-dimensional material nanophotonics. *Nat. Photon.* **8**, 899–907 (2014).
- Jakšić, Z. *Micro and Nanophotonics for Semiconductor Infrared Detectors* (Springer, Basel, 2014).
- Rogalski, A., Adamiec, K. & Rutkowski, J. *Narrow-Gap Semiconductor Photodiodes* (SPIE, Bellingham, WA, 2000).
- Wang, X., Cheng, Z., Xu, K., Tsang, H. K. & Xu, J.-B. High-responsivity graphene/silicon-heterostructure waveguide photodetectors. *Nat. Photon.* **7**, 888–891 (2013).
- Xia, F., Wang, H. & Jia, Y. Rediscovering black phosphorus as an anisotropic layered material for optoelectronics and electronics. *Nat. Commun.* **5**, 5458 (2014).
- Ling, X., Wang, H., Huang, S., Xia, F. & Dresselhaus, M. S. The renaissance of black phosphorus. *Proc. Natl Acad. Sci. USA* **112**, 4523–4530 (2015).
- Yuan, H. et al. Polarization-sensitive broadband photodetector using a black phosphorus vertical p–n junction. *Nat. Nanotech.* **10**, 707–713 (2015).
- Qiao, J., Kong, X., Hu, Z.-X., Yang, F. & Ji, W. High-mobility transport anisotropy and linear dichroism in few-layer black phosphorus. *Nat. Commun.* **5**, 5475 (2014).
- Hong, T. et al. Anisotropic photocurrent response at black phosphorus– $\text{MoS}_2$  p–n heterojunctions. *Nanoscale* **7**, 18537–18541 (2015).
- Deng, Y. et al. Black phosphorus–monolayer  $\text{MoS}_2$  van der Waals heterojunction p–n diode. *ACS Nano* **8**, 8292–8299 (2014).
- Ye, L., Li, H., Chen, Z. & Xu, J. Near-infrared photodetector based on  $\text{MoS}_2$ /black phosphorus heterojunction. *ACS Photon.* **3**, 692–699 (2016).
- Chen, P. et al. Gate tunable  $\text{WSe}_2$ –BP van der Waals heterojunction devices. *Nanoscale* **8**, 3254–3258 (2016).
- Shim, J. et al. Phosphorene/rhenium disulfide heterojunction-based negative differential resistance device for multi-valued logic. *Nat. Commun.* **7**, 13413 (2016).
- Huang, M. et al. Broadband black-phosphorus photodetectors with high responsivity. *Adv. Mater.* **28**, 3481–3485 (2016).
- Youngblood, N., Chen, C., Koester, S. J. & Li, M. Waveguide-integrated black phosphorus photodetector with high responsivity and low dark current. *Nat. Photon.* **9**, 247–252 (2015).
- Guo, Q. et al. Black phosphorus mid-infrared photodetectors with high gain. *Nano Lett.* **16**, 4648–4655 (2016).
- Mao, N. et al. Optical anisotropy of black phosphorus in the visible regime. *J. Am. Chem. Soc.* **138**, 300–305 (2016).
- Liu, H. et al. Phosphorene: an unexplored 2D semiconductor with a high hole mobility. *ACS Nano* **8**, 4033–4041 (2014).
- Tran, V., Soklaski, R., Liang, Y. & Yang, L. Layer-controlled band gap and anisotropic excitons in few-layer black phosphorus. *Phys. Rev. B* **89**, 235319 (2014).
- Li, D. et al. Polarization and thickness dependent absorption properties of black phosphorus: new saturable absorber for ultrafast pulse generation. *Sci. Rep.* **5**, 15899 (2015).
- Macleod, A. *Thin-Film Optical Filters* (CRC, Boca Raton, FL, 2010).
- Villegas, C. E. P., Rocha, A. R. & Marini, A. Anomalous temperature dependence of the band gap in black phosphorus. *Nano Lett.* **16**, 5095–5101 (2016).
- Villegas, C. E. P., Rodin, A. S., Carvalho, A. & Rocha, A. R. Two-dimensional exciton properties in monolayer semiconducting phosphorus allotropes. *Phys. Chem. Chem. Phys.* **18**, 27829–27836 (2016).
- Li, L. et al. Quantum Hall effect in black phosphorus two-dimensional electron system. *Nat. Nanotech.* **11**, 593–597 (2016).
- Martyniuk, P., Kopytko, M. & Rogalski, A. Barrier infrared detectors. *Opto-Electron. Rev.* **22**, 127–146 (2014).
- Dhar, N. K., Dat, R. & Sood, A. K. in *Optoelectronics—Advanced Materials and Devices* Ch. 7 (InTech, London, 2013).
- Amani, M., Regan, E., Bullock, J., Ahn, G. H. & Javey, A. Mid-wave infrared photoconductors based on black phosphorous–arsenic alloys. *ACS Nano* **11**, 11724–11731 (2017).
- Buscema, M. et al. Fast and broadband photoresponse of few-layer black phosphorus field-effect transistors. *Nano Lett.* **14**, 3347–3352 (2014).
- Martyniuk, P. & Rogalski, A. HOT infrared photodetectors. *Opto-Electron. Rev.* **21**, 239–257 (2013).
- Yau, L. D. & Sah, C.-T. Theory and experiments of low-frequency generation–recombination noise in MOS transistors. *IEEE Trans. Electron. Devices* **16**, 170–177 (1969).
- Long, M. et al. Room temperature high-detectivity mid-infrared photodetectors based on black arsenic phosphorus. *Sci. Adv.* **3**, e1700589 (2017).
- Haddadi, A., Dehngani, A., Chevallier, R., Adhikary, S. & Razezghi, M. Bias-selectable nBn dual-band long-/very long-wavelength infrared photodetectors based on  $\text{InAs}/\text{InAs}_{1-x}\text{Sb}_x/\text{AlAs}_{1-x}\text{Sb}_x$  type-II superlattices. *Sci. Rep.* **7**, 3379 (2017).
- Bullock, J., Cuevas, A., Allen, T. & Battaglia, C. Molybdenum oxide  $\text{MoO}_x$ : a versatile hole contact for silicon solar cells. *Appl. Phys. Lett.* **105**, 232109 (2014).
- Chuang, S. et al.  $\text{MoS}_2$  p-type transistors and diodes enabled by high work function  $\text{MoO}_x$  contacts. *Nano Lett.* **14**, 1337–1342 (2014).

## Acknowledgements

The authors thank P. Wijewarnasuriya and E. DeCuir from the US Army Research Laboratory for discussions. This work was supported by the Defence Advanced Research Projects Agency under contract no. HR0011-16-1-0004. K.B.C. acknowledges funding

from the Australian Research Council (DP150103736 and FT140100577) and an Innovation Fellowship from the Victorian Endowment for Science, Knowledge and Innovation (VESKI).

### Author contributions

J.B., M.A. and A.J. conceived the idea for the project and designed the experiments. J.B. and M.A. performed optical measurements. M.A., J.B., J.C. and G.H.A. fabricated devices. V.A. performed device simulations. Y.-Z.C. and Y.-L.C. performed TEM measurements. J.B., M.A., V.A., V.R.S., Y.G., K.B.C. and A.J. analysed the data. J.B., M.A. and A.J. wrote the manuscript. All authors discussed the results and commented on the manuscript.

### Competing interests

The authors declare no competing interests

### Additional information

**Supplementary information** is available for this paper at <https://doi.org/10.1038/s41566-018-0239-8>.

**Reprints and permissions information** is available at [www.nature.com/reprints](http://www.nature.com/reprints).

**Correspondence and requests for materials** should be addressed to A.J.

**Publisher's note:** Springer Nature remains neutral with regard to jurisdictional claims in published maps and institutional affiliations.

## Methods

**Refractive index extraction and optical simulations.** Samples for refractive index extraction were fabricated by thermally evaporating Ti/Au (5/80 nm) onto a Si/SiO<sub>2</sub> carrier wafer. Following this, bP (Smart Elements) was mechanically exfoliated onto the Au surface in an N<sub>2</sub> purged glovebox. A set of 22 bP flakes were chosen with approximately linearly spaced thickness from 50 to 500 nm, as measured by atomic force microscopy (AFM) (Bruker Dimension Icon). Polarized reflection measurements were taken using a FTIR microscope (Thermo Scientific, Nicolet iS50) with a BaF<sub>2</sub> wire grid linear polarizer (Thorlabs). The armchair direction of the bP absorber was determined by measuring reflection as a function of polarization, to find the angle at which maximum absorption occurs. Implicit in this approach is the assumption that the largest absorption will occur when light is aligned to the *x*, or armchair, direction, a fact that has been theoretically predicted and demonstrated by a number of previous studies<sup>7,35,36</sup>. In all cases the minimum absorption (at 0.31 eV) was found to be offset by 90° from this angle, corresponding to the expected zigzag or *y* direction. All FTIR reflection measurements in this study utilize a bare Au surface as a 100% reflection standard. The set of reflection curves in the *x* direction were fitted using the transfer matrix method, which models the reflection of the bP/Au stack using the refractive indices of bP as the only fitting parameter. Optical simulations of the full bP/MoS<sub>2</sub>/Au photodiodes were also performed through the transfer matrix method utilizing known refractive index values for Au, constant values for MoS<sub>2</sub> ( $n = 4.3$ ,  $k = 0$ ), as well as the refractive index values for bP measured in this work. An average of the bP absorption values over the  $\lambda = 2.5\text{--}3.8\ \mu\text{m}$  range was obtained for every combination of MoS<sub>2</sub> and bP thicknesses.

**Device fabrication.** The photodiodes presented in this work were fabricated by a dry transfer process utilizing a poly(methyl methacrylate) (PMMA) carrier. A detailed description of this process is provided in Supplementary Section 2. In brief, freshly exfoliated bP and MoS<sub>2</sub> sheets were transferred onto an Au pad, creating an Au/bP/MoS<sub>2</sub> stack. A contact to the MoS<sub>2</sub> layer was then patterned by electron-beam lithography and a 40-nm-thick Ni film was subsequently deposited by thermal evaporation. In some devices, the heterojunction was patterned by electron-beam lithography and subsequently etched in a Xactix vapour etching tool by XeF<sub>2</sub> (ref. <sup>37</sup>). Finished devices were encapsulated by an ~2-nm-thick AlO<sub>x</sub> layer formed by thermal evaporation of Al. Example micrographs taken during the above process steps are provided in Supplementary Fig. 2. A discussion of the assumptions made for the area of the device is provided in Supplementary Section 2.

For the polarization-resolved detector, an identical dry transfer process was used to create a MoS<sub>2</sub>/bP/Au stack. An additional bP flake was transferred on top of the MoS<sub>2</sub> layer so that its crystal orientation was orthogonal to the bottom bP layer. The crystalline orientations of the bP sheets were determined using polarized reflection measurements performed in an FTIR microscope as described above. The hole contact for the top bP device was patterned using electron-beam lithography, followed by evaporation of MoO<sub>3</sub>/Pd (4/30 nm). For all devices in this study, care was taken to reduce air exposure during the fabrication of devices to minimize PO<sub>x</sub> growth at the bP surface. Processing steps, including bP exfoliation, liftoff, PMMA removal and AFM, were all performed in either a glovebox or a nitrogen purged environment, and all chemicals used were anhydrous. For measurements of surface oxidation prevention in fabricated devices see Supplementary Section 3.

**Device characterization.** Finished devices were wire-bonded into 24-pin chip-carriers, which were in turn mounted into a cryostat with a CaF<sub>2</sub> window and measured at a base pressure  $<1 \times 10^{-5}$  torr. Current–voltage measurements were taken in a two-probe configuration under vacuum using an Agilent Technologies B1500A semiconductor device analyser. The spectral response and  $\eta_e$  were characterized at  $I_{sc}$  (0 V bias) by placing the cryostat at the auxiliary exit port of the FTIR. The sample was then excited using modulated illumination from a Global (1,000 K blackbody). The resulting photocurrent was then sent to a current amplifier (Stanford Research Systems SRS570) and subsequently returned to the external detector interface of the FTIR. For polarization-resolved measurements, a BaF<sub>2</sub> wire grid linear polarizer was placed in the beam path. The FTIR system was calibrated using two reference detectors: a NIST calibrated Ge photodiode was used to measure the source intensity at the outlet and an in-built deuterated-triglycine sulfate (DTGS) detector was used to measure the relative spectral intensity of the source. Further information on the FTIR set-up is provided in Supplementary Section 3. Additionally, the detectivity values were confirmed using a blackbody set-up with flood illumination. Here the device was excited using a chopper-modulated blackbody (Omega BB703, temperature range 473–673 K) with no additional optics besides the cryostat window; the incident power density was calculated using Planck's law and geometrical considerations (aperture size and sample to blackbody distance). Further details on this process are provided in Supplementary Section 4 and in ref. <sup>27</sup>. Reflection measurements were performed in an attached FTIR microscope, with the wire grid polarizer placed in the incoming beam path. The rise/fall times and linearity of the device were characterized using illumination from a  $\lambda = 2.7\ \mu\text{m}$  laser diode (Brolis Semiconductors). For rise/fall measurements the laser diode was directly modulated with a square waveform (Agilent 33120A), and the instrument response was measured using a commercial InAs photodiode (Judson Technologies). For frequency response measurements a SRS570 current amplifier in high-bandwidth mode with a gain of  $>20\ \mu\text{A V}^{-1}$  was used (corresponding to a bandwidth of 1 MHz). For dynamic range measurements the laser was directly modulated at a frequency of 120 Hz. The photocurrent was measured using a lock-in amplifier (Stanford Research Systems SR865). The laser diode intensity was adjusted over a five order of magnitude dynamic range by controlling the laser current (ThorLabs ITC4002QCL) in combination with the use of neutral density filters in the beam path. The 3 dB frequency analysis was performed with a  $\lambda = 1.6\ \mu\text{m}$  laser diode (ThorLabs), directly modulated with a sinusoidal waveform (Agilent 33120A).

**Data availability.** The data that support the plots within this paper and other findings of this study are available from the corresponding author upon reasonable request.

## References

- Low, T. et al. Tunable optical properties of multilayer black phosphorus thin films. *Phys. Rev. B* **90**, 075434 (2014).
- Morita, A. Semiconducting black phosphorus. *Appl. Phys. A* **39**, 227–242 (1986).
- Huang, Y. et al. An innovative way of etching MoS<sub>2</sub> characterization and mechanistic investigation. *Nano Res.* **6**, 200–207 (2013).